

Atom interferometry in a marginally stable optical resonator

I. Riou^{1,5}†, N. Mielec^{2,5}†, G. Lefèvre^{1,5}, M. Prevedelli³, A. Landragin^{2,5}, P. Bouyer^{1,5}, A. Bertoldi^{1,5}, R. Geiger^{2,5}, and B. Canuel^{1,4,5}

E-mail: remi.geiger@obspm.fr, benjamin.canuel@institutoptique.fr

¹LP2N, Laboratoire Photonique, Numérique et Nanosciences, Université Bordeaux–IOGS–CNRS:UMR 5298, rue F. Mitterrand, F–33400 Talence, France.

²LNE–SYRTE, Observatoire de Paris, PSL Research University, CNRS, Sorbonne Universités, UPMC Univ. Paris 06, 61 avenue de l’Observatoire, F–75014 Paris, France.

³Dipartimento di Fisica e Astronomia, Università di Bologna, Via Bertini-Pichat 6/2, I–40126 Bologna, Italy.

⁴LSBB, Laboratoire Souterrain à Bas Bruit UNS, UAPV, CNRS:UMS 3538, AMU, La Grande Combe, F–84400 Rustrel, France.

⁵MIGA Consortium

Abstract. We propose a marginally stable optical resonator suitable for atom interferometry. The resonator geometry is based on two flat mirrors at the focal planes of a lens that produces the large beam waist required to coherently manipulate cold atomic ensembles. Optical gains of about 100 are achievable with optics of part-per-thousand losses. The resulting power build-up will allow for enhanced coherent manipulation of the atomic wavepackets. We study the effect of longitudinal misalignments and assess the robustness of the resonator in terms of intensity and phase profiles of the intra-cavity field. We also study how to implement atom interferometry based on large momentum transfer Bragg diffraction in such cavity.

1. Introduction

Optical cavities have been extensively adopted in cold neutral atom physics to mediate the interaction between radiation and matter. For instance, cavity quantum electrodynamics (QED) studies the coupling of atoms with the light in an optical resonator [1, 2], and cavity tailored spontaneous emission probability of atomic ensembles is at the basis of self-organization and superradiance phenomena [3, 4]. Optical cavities have been used to produce BECs in the strong-coupling regime for single atoms [5], and to entangle the particles of an atomic ensemble to mitigate the noise related to counting them beyond the so-called standard quantum limit [6, 7].

† Both authors contributed equally to this work.

Recently, an atom interferometer has been realized using a vertical optical cavity [8]. This approach provides power enhancement and spatial filtering for the beamsplitters, with potential advantages in terms of both sensitivity and accuracy. An increased intensity of the interrogation laser beams, thanks to the cavity build up, can be exploited to increase the scale factor of atomic inertial sensors by using coherent multiphoton processes [9, 10, 11, 12]. Such Large Momentum Transfer (LMT) techniques impose constraints on the laser power, because of their velocity selectivity in relation to the Doppler effect experienced by the atoms at finite temperature. For example, a LMT beam splitter of order n requires a laser intensity scaling as n^4 at fixed spontaneous emission rate [13]. Moreover, an interferometric control of the beam splitter wavefront could reduce the systematic effects introduced by beam distortions [14]; more precisely, using an optical cavity to filter the laser mode moves the problem to the quality of the mirrors implementing the resonator.

State-of-the-art precision measurements setups based on atom interferometry such as gyroscopes [15] or gravimeters [16, 17] make use of atom sources cooled to the μK level. In these devices, atom clouds may reach cm-scale size during the interferometric sequence because of thermal expansion, making efficient implementation of cavity-enhanced beam splitters challenging.

In this paper, we propose to use a marginally stable optical resonator including a focusing element that can give a mode of several millimeters in diameter. Stability of this cavity depends critically on the relative distance between the optical elements of the resonator. In the context of atom interferometry, longitudinal alignment errors have to be carefully investigated as they introduce phase distortions of the mode which might impact the sensitivity and accuracy of the measurement. We first introduce the geometry and main features of the resonator. We calculate then the intracavity field as a function of alignment errors, carrying out the computations with an iteration code based on the propagation of paraxial rays using the ABCD formalism [18]. We finally numerically simulate a Bragg atom interferometer with cold atoms to assess the feasibility of LMT atom optics enhanced with this resonator.

2. A resonator for atom interferometry

In the following, we introduce the requirements that will drive the design of a resonator where the cavity stationary field will be used to create an interferometer for matter-waves based on $2n$ -photons Bragg transitions. We consider as an example that the resonator will be used to interrogate a source of rubidium atoms at a temperature of $T_e=1\ \mu\text{K}$ using a set of laser pulses applied up to a time $t_{\text{free}} = 250\ \text{ms}$ after preparation. In this time-window, the dispersion in position of the atom cloud will be characterized by a Gaussian distribution of maximum $1/e^2$ width of $t_{\text{free}}\sqrt{kT_e/M}=5\ \text{mm}$, where k is the Boltzmann constant and M the mass of an atom. In the following, we will therefore take as guideline that the cavity has to be resonant with a fundamental Gaussian beam of waist $\omega_0=5\ \text{mm}$. In order to be easily integrated on common AI experiments [16, 17] we

also set the maximum cavity length to be $L = 1$ m. As a resonance criteria we consider that the complex radius of curvature describing the Gaussian beam $q_0 = iz_{r0} + z_0$ (where $z_{r0} = \frac{\pi\omega_0^2}{\lambda}$ is the Rayleigh length and z_0 the waist location) has to remain invariant on a cavity round trip.

Using a common two mirror geometry, the only resonators that can match this resonance criteria are:

- Strictly stable cavities that are resonant with a unique Gaussian beam whose waist size and position are set by the radius of curvature of the cavity mirrors.
- Marginally stable confocal cavities that are resonant with any Gaussian beams, given that the cavity mirrors match the confocal criteria.

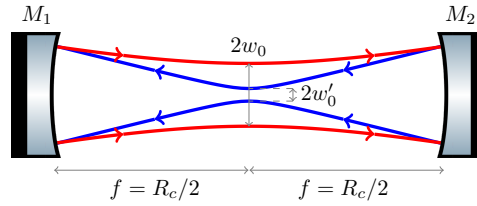


Figure 1. A confocal cavity can be made resonant with a Gaussian beam of waist $\omega_0=5$ mm located at the center of the cavity and propagating in the forward direction (red). The resonating field propagating in the backward direction is then a Gaussian beam of waist $\omega'_0 = \frac{\lambda R_c/2}{\pi\omega_0}$ (blue).

Reducing the discussion to symmetric resonators, a strictly stable cavity of length L resonant with a Gaussian beam of waist $\omega_0=5$ mm would have mirrors of radius of curvature of $R_c > 20$ km, putting extremely stringent requirements on the quality of cavity optics[‡], which rules out this configuration. The last possibility is then to use a confocal cavity with mirrors of radius of curvature $R_c = L/2$ as illustrated in Fig.1. In this marginally stable configuration, the cavity could be made resonant with a Gaussian beam of waist $\omega_0=5$ mm traveling in the forward direction but the Gaussian beam traveling in the backward direction would be strongly focused with an image waist $\omega'_0 = \frac{\lambda R_c/2}{\pi\omega_0} < 20 \mu\text{m}$, which would spoil the atom interrogation process.

The design of such a resonator for atom interferometry therefore requires to look further than the simple two mirrors geometry.

2.1. Description of the cavity

We propose to use a resonator geometry presented on Fig. 2: two flat mirrors (M_1) and (M_2) placed at the focal point of an intra-cavity lens (l). This resonator has a round-trip

[‡] The sag of the curved mirror surface for a one inch optics would be smaller than 4 nm which represents a deviation from a perfectly flat surface smaller than $\lambda/200$.

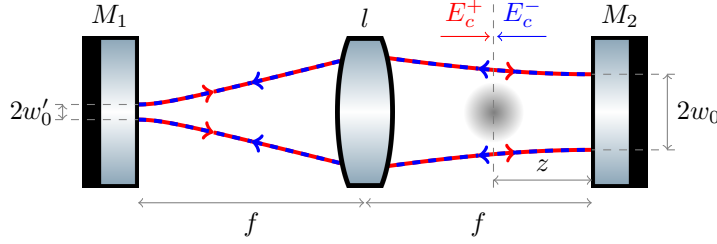


Figure 2. Geometry of the proposed resonator with one lens of focal length f placed at the center of parallel-plane cavity of length $2f$. An input Gaussian beam of waist ω'_0 located on (M_1) is imaged on (M_2) with a magnification factor $\lambda f/(\pi\omega_0'^2)$. The atom source is placed at distance z from (M_2).

ABCD transfer matrix [19] of:

$$T = \begin{pmatrix} 1 & f \\ 0 & 1 \end{pmatrix} \begin{pmatrix} 1 & 0 \\ -1/f & 1 \end{pmatrix} \begin{pmatrix} 1 & 2f \\ 0 & 1 \end{pmatrix} \begin{pmatrix} 1 & 0 \\ -1/f & 1 \end{pmatrix} \begin{pmatrix} 1 & f \\ 0 & 1 \end{pmatrix} = \begin{pmatrix} -1 & 0 \\ 0 & -1 \end{pmatrix} = -Id \quad (1)$$

meaning that any complex radius of curvature describing a Gaussian beam $q = iz_r + z$ will be transformed back to itself after one round trip inside the cavity. This property is specific to marginally stable resonators such as the symmetric confocal cavity presented in Fig. 1. In particular, when the resonator is injected with a Gaussian beam of waist ω'_0 placed on the input mirror (M_1) the lens forms its image waist $\omega_0 = \frac{\lambda f}{\pi\omega'_0}$ on the mirror (M_2) which forms back the image of the initial waist ω'_0 on (M_1). In comparison with the configuration of Fig. 1, this resonator has an unfolded geometry which enables to have identical forward and backwards resonating Gaussian beams.

We note that a configuration with similar properties has been extensively studied in the context of high precision spectroscopy before the advent of cold atoms, in order to obtain large interrogation beams to reduce the transit broadening [20]. In such work, the focusing element was a parabolic reflector collimating the light coming from its focus on a flat mirror. The use of a lens has the advantage to obtain a resonator with a fully cylindrical symmetry, which is more robust to alignment issues.

In the following, we will set $f = 40$ cm and $\omega'_0 = 20$ μ m which enables to obtain an image waist of $\omega_0 = 5$ mm which complies with the requirements of Sec. 2

2.2. Calculation of the cavity interrogation fields

During the interrogation process based on Bragg transitions, the atoms located at a distance z from (M_2) will be diffracted on the standing wave created by the counter-propagating cavity fields $E_c^\pm(r, z) = |E_c^\pm(r, z)|e^{i\varphi^\pm(r, z)}$ at position of the atom source. We now calculate longitudinal and transverse dependence of the product of the fields modulus $|E_c^+(r, z)E_c^-(r, z)|$ and their phase difference $\Delta\phi(r, z) = \varphi^+(r, z) - \varphi^-(r, z)$ that can respectively limit atom diffraction efficiency and introduce spurious measurement biases. These aspects we be will studied futher in Sec.3.

As $E_c^\pm(r, z)$ are Gaussian fields at a distance $\mp z$ from the waist ω_0 located on (M_2) , they may be expressed analytically as:

$$E_c^\pm(r, z) = \sqrt{\frac{4\mu_0 c P_c^\pm}{\pi}} \frac{1}{\omega(z)} e^{-\frac{r^2}{\omega(z)^2}} e^{\mp i\phi_G(z)} e^{\pm i\frac{kr^2}{2R_c(z)}} \quad (2)$$

where $\omega(z) = \sqrt{\omega_0^2 \left[1 + \left(\frac{z}{z_{r0}}\right)^2\right]}$, $R_c(z) = z + \frac{z_{r0}^2}{z}$ and $\phi_G(z) = \arctan\left(\frac{z}{z_{r0}}\right)$ are respectively the waist size, the radius of curvature and the Gouy phase of the Gaussian beam at position of the atoms. We also define μ_0 as the vacuum permeability, c as the light velocity in vacuum and P_c^\pm as the power of the E_c^\pm fields. We therefore obtain:

$$|E_c^+(r, z) E_c^-(r, z)| = \frac{4\mu_0 c G P_{in}}{\pi w(z)^2} e^{\frac{-2r^2}{w(z)^2}} \quad (3)$$

$$\Delta\phi(r, z) = \frac{-2kr^2}{2R_c(z)} + 2\phi_G(z). \quad (4)$$

Where G is the amplification factor of the cavity defined as $G = \sqrt{P_c^+ P_c^-} / P_{in}$ that will be a key parameter for LMT applications.

The optical gain G can be expressed as a function of cavity parameters: if we note r_1, r_2, r_L the amplitude reflection coefficients of respectively (M_1) , (M_2) and (l) that we consider without losses, G becomes (see [Appendix A](#)):

$$G = \frac{r_2(1 - r_1^2)(1 - r_L^2)}{(1 - r_1 r_2(1 - r_L^2))^2}. \quad (5)$$

For a cavity formed with identical mirrors, Fig. 3 shows the amplification factor as a function of squared reflectivities of (M_1) and (M_2) for lens reflections r_L^2 between 500 ppm and 4000 ppm. We observe that optical gain of a few hundreds can be achieved by using an intra-cavity lens with standard anti-reflection treatments.

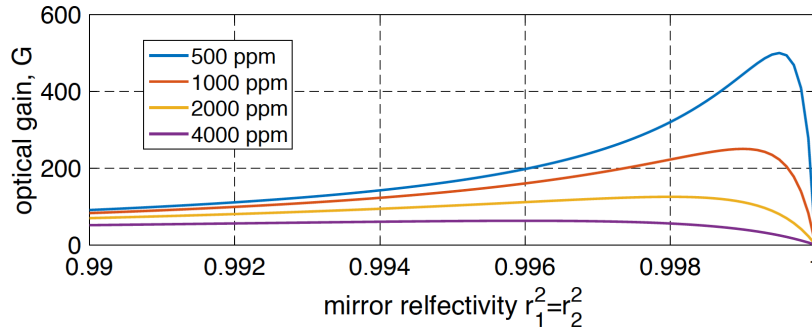


Figure 3. Amplification factor of the resonator with respect to the reflectivity of its mirrors for different transmission values of the intra-cavity lens.

In the following, we will set $r_L^2 = 1000$ ppm and $r_1^2 = r_2^2 = 0.9912$. These settings yield an optical gain of $G = 100$ and a Finesse of $\mathcal{F} = 355$.

2.3. Influence of longitudinal misalignments

Longitudinal misalignments of the optical elements with respect to the ideal $f - f$ configuration will make the resonator strictly stable or unstable and thus modify its resonating field for the same input Gaussian beam. If the distance between (l) and ($M_{1,2}$) is changed to $f + \delta_{1,2}$, the round-trip ABCD matrix of the cavity becomes:

$$T' = \begin{pmatrix} -1 + \frac{2\delta_1\delta_2}{f^2} & 2\delta_1(-1 + \frac{2\delta_1\delta_2}{f^2}) \\ \frac{2\delta_2}{f^2} & -1 + \frac{2\delta_1\delta_2}{f^2} \end{pmatrix} = \begin{pmatrix} A & B \\ C & D \end{pmatrix}. \quad (6)$$

The resonator will be strictly stable if $|A + D| < 2$ and unstable if $|A + D| > 2$. In other words, the resonator will be strictly stable if δ_1 and δ_2 have the same sign, and unstable if they have opposite signs (the ideal case $\delta_1 = \delta_2 = 0$ corresponding to the marginally stable configuration).

While calculation of the resonating field in the strictly stable case can be again evaluated analytically in terms of decomposition of the input beam on the cavity modes, the mathematical description of the resonator in the unstable case is more complex [21]. In the following, we introduce a formalism to calculate the resonating field in all stability conditions and study variation of phase and amplitude of the resonating field as a function of misalignments $\delta_{1,2}$. In practice such misalignments could result from temperature fluctuations, vibrations or imprecisions in the cavity assembling. We will show that the properties of the intra-cavity field will only be slightly modified for the typical misalignments ($\delta_{1,2} \sim 10 \mu m$) which might be experimentally encountered, and that such imperfections are thus not critical for atom interferometry applications.

2.3.1. Calculation of the interrogation field taking into account longitudinal misalignments. We calculate in an iterative way the field resonating in the cavity at position of the atoms. Our method is based on ABCD-matrix propagation of the input Gaussian beam through its round-trip inside the resonator. In the following, we note q_n^\pm the complex radius of curvature of the Gaussian beam at position of the atoms in the forward (+) and backwards (-) directions after n round trips inside the cavity. For the

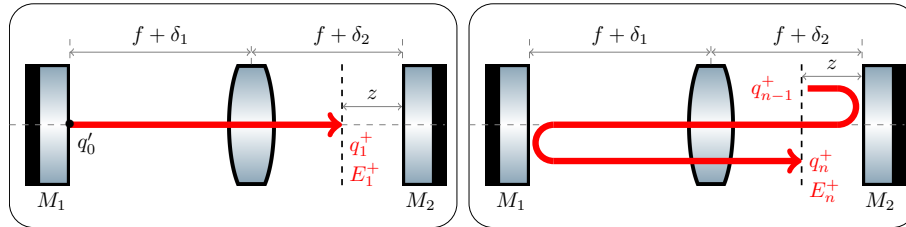


Figure 4. Determination of the q^+ parameter for the field propagating to the right: for the first round trip (left), and for the n th round trip with $n > 1$ (right).

first round trip, q_1^+ is obtained from the input beam $q_0^+ = i \frac{\pi(\omega_0')^2}{\lambda}$ by using the ABCD

transfer matrix (see Fig. 4-left):

$$U = \begin{pmatrix} 1 & \delta_2 + f - z \\ 0 & 1 \end{pmatrix} \begin{pmatrix} 1 & 0 \\ -1/f & 1 \end{pmatrix} \begin{pmatrix} 1 & \delta_1 + f \\ 0 & 1 \end{pmatrix} \quad (7)$$

Then for the n th round trip with $n > 1$, the complex radius of curvature q_n^+ is obtained from q_{n-1}^+ using the transfer matrix (see Fig. 4-right):

$$V = \begin{pmatrix} 1 & \delta_2 + f - z \\ 0 & 1 \end{pmatrix} \begin{pmatrix} 1 & 0 \\ -1/f & 1 \end{pmatrix} \begin{pmatrix} 1 & 2(\delta_1 + f) \\ 0 & 1 \end{pmatrix} \begin{pmatrix} 1 & 0 \\ -1/f & 1 \end{pmatrix} \begin{pmatrix} 1 & z + \delta_2 + f \\ 0 & 1 \end{pmatrix} \quad (8)$$

For all round trips, the complex radius of curvature of the beam propagating in the

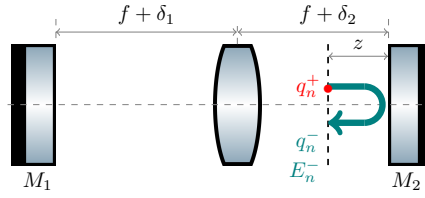


Figure 5. Determination of the q^- parameter for the field propagating to the left.

backwards direction q_n^- can be obtained from q_n^+ using the transfer matrix (see Fig. 5):

$$W = \begin{pmatrix} 1 & 2z \\ 0 & 1 \end{pmatrix}. \quad (9)$$

We therefore obtain the following iterative expression for q_n^\pm :

$$\begin{cases} q_1^+ = \frac{U_{11} \cdot q_0 + U_{12}}{U_{21} \cdot q_0 + U_{22}} \\ q_n^+ = \frac{V_{11} \cdot q_{n-1}^+ + V_{12}}{V_{21} \cdot q_{n-1}^+ + V_{22}} & \text{for } n > 1 \\ q_n^- = \frac{W_{11} \cdot q_n^+ + W_{12}}{W_{21} \cdot q_n^+ + W_{22}} & \text{for } n \geq 1. \end{cases} \quad (10)$$

We then obtain the expression of beam size ω_n^\pm and real radius of curvature R_n^\pm of the gaussian beam at position of the atoms in the forward (+) and backwards (-) directions after n round trips inside the cavity:

$$\begin{cases} \omega_n^\pm = \sqrt{\frac{-\lambda}{\pi \text{Im}(1/q_n^\pm)}} \\ R_n^\pm = \frac{1}{\text{Re}(1/q_n^\pm)} \end{cases} \quad (11)$$

The accumulated Gouy phase shift $\phi_{G,n}^{\text{acc}\pm}$ can then be calculated in an iterative way [22] considering that the phase reference is taken in the plane of q_1^+ , ie. $\phi_{G,1}^{\text{acc}+} = 0$

$$\begin{cases} \phi_{G,1}^{\text{acc}+} = 0 \\ \phi_{G,n}^{\text{acc}+} = \phi_{G,n-1}^{\text{acc}+} + \tan^{-1} \left(\frac{\lambda V_{12}}{\left(V_{11} + \frac{V_{12}}{R_{n-1}^+}\right) \pi (\omega_{n-1}^+)^2} \right) & \text{for } n > 1 \\ \phi_{G,n}^{\text{acc}-} = \phi_{G,n-1}^{\text{acc}-} + \tan^{-1} \left(\frac{\lambda W_{12}}{\left(V_{11} + \frac{W_{12}}{R_{n-1}^-}\right) \pi (\omega_{n-1}^-)^2} \right) & \text{for } n \geq 1 \end{cases} \quad (12)$$

The Gaussian field $E_n^\pm(r, z)$ at position of the atom after n round trips can then be expressed:

$$\begin{cases} E_n^+(r, z) = t_1 t_L (r_1 r_2 t_L^2)^{n-1} \sqrt{\frac{4\mu_0 c P_{\text{in}}}{\pi}} \frac{1}{w_n^+} e^{-\frac{r^2}{(w_n^+)^2}} e^{-2iknL} e^{i\phi_{G,n}^{\text{acc}+}} e^{-i\frac{kr^2}{2R_n^+}} \\ E_n^-(r, z) = t_1 t_L r_2 (r_1 r_2 t_L^2)^{n-1} \sqrt{\frac{4\mu_0 c P_{\text{in}}}{\pi}} \frac{1}{w_n^-} e^{-\frac{r^2}{(w_n^-)^2}} e^{-2ik(nL+z)} e^{i\phi_{G,n}^{\text{acc}-}} e^{-i\frac{kr^2}{2R_n^-}} \end{cases} \quad (13)$$

where $L = 2f + \delta_1 + \delta_2$ is the length of the cavity and $k = 2\pi/\lambda$ is the wave number. The total intra-cavity field $E_c^\pm(r, z)$ is the interference of the fields $E_n^\pm(r, z)$:

$$E_c^\pm(r, z) = \sum_{n=1}^N E_n^\pm(r, z). \quad (14)$$

2.3.2. Study of the influence of misalignments. We now use the above method to calculate numerically $|E_c^+(r, z)E_c^-(r, z)|$ and $\Delta\phi(r, z)$ for different longitudinal misalignments $\delta_{1,2}$. For each value of $\delta_{1,2}$, we calculate numerically the sum of Eq. (14) maximizing the power in transmission of the cavity by changing the input wavelength. This last criteria ensures that the cavity is locked correctly (see [Appendix B](#) for details of the simulation).

Fig. 6 shows the results of the calculation for various displacements δ_1 of the input mirror with respect to the ideal configuration while keeping $\delta_2 = 0$. Panel (a) shows the field intensity profiles of the two counter-propagating cavity fields at the atom position, and panel (b) their relative phase. When the resonator is perfectly aligned ($\delta_1 = \delta_2 = 0$), the fields are Gaussian with an almost uniform relative phase. In this ideal alignment configuration, we verified that the results of the numerical calculation give the same results as the analytic expressions of Eq. (3) and (4). The displacement of the input mirror determines a ring-shaped intensity distribution of the cavity fields, and increases the inhomogeneity of their relative phase. These inhomogeneities are due to the fact that the fields do not perfectly overlap after each round-trip and acquire a spatially-dependent phase shift. Moreover, misalignments degrade the optical gain that does not reach anymore the maximum value of $G = 100$ given by Eq. 5. Precisely, the optical gain equals 100, 80, 66, 42 for $\delta_1 = 0, 10, 20, 50 \mu\text{m}$, respectively. The drop of the gain results from the progressive dephasing of the fields after each round trip.

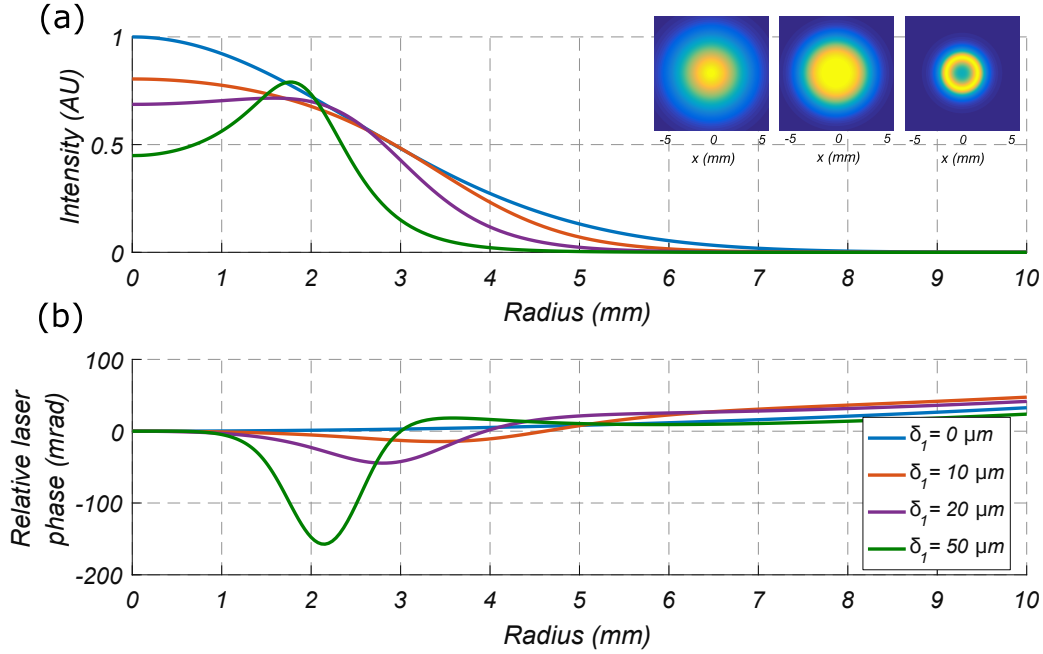


Figure 6. (a) Radial intensity profile of the cavity field $E_c^+(r, z)$ at the middle point z between the lens and the mirror M_2 , for various misalignments $\delta_1 = 0, 10, 20, 50 \mu\text{m}$. The intensity profiles are normalized to the maximum achievable intensity in the case of the ideal configuration, corresponding to $G = 100$. Inset: 2D plot of the corresponding normalized intensity cross-section for 0, 20, 50 μm . (b) Radial profile of the relative phase $\Delta\phi(r, z)$ between the two counter-propagating cavity fields $E_c^+(r, z)$ and $E_c^-(r, z)$.

Finally, displacements δ_2 of the back mirror (M_2) have little impact on the intensity and phase profile of the intra-cavity fields compared to the displacements of (M_1) (see [Appendix C](#)). Indeed, from the side of (M_2) the fields are close to plane waves and variations of δ_2 therefore have small impact on their transverse phase dependence.

In the next section, we will discuss the influence of the distortions of the intra-cavity fields on the performances of the atom interferometer.

3. Large momentum transfer atom interferometry

3.1. Configuration

We consider an atom interferometer that exploits the optical gain of our resonator to enhance its sensitivity via LMT techniques. If the interferometer is operated on ground, the atomic ensemble moves with respect to the cavity setup because of the gravitational acceleration. Two configurations can be adopted. First, a vertical interrogation cavity with the atoms moving along its axis, as in [8]. A systematic effect to be considered in that case is the different laser phases experienced by the atoms along the cavity axis during their displacement. A second configuration can be adopted, based instead on a horizontal interrogation [15]. The motion of the atomic clouds along the gravity

axis imposes in that case an interrogation cavity at each position where the atoms are manipulated. In the case of a $\pi/2 - \pi - \pi/2$ light pulse sequence with the π pulse at the apogee of the trajectory (as in [23]), then two vertically separated horizontal cavities are required. The two interrogation cavities must be aligned and stabilized with high precision to control systematic effects and to maintain the fringe visibility [15].

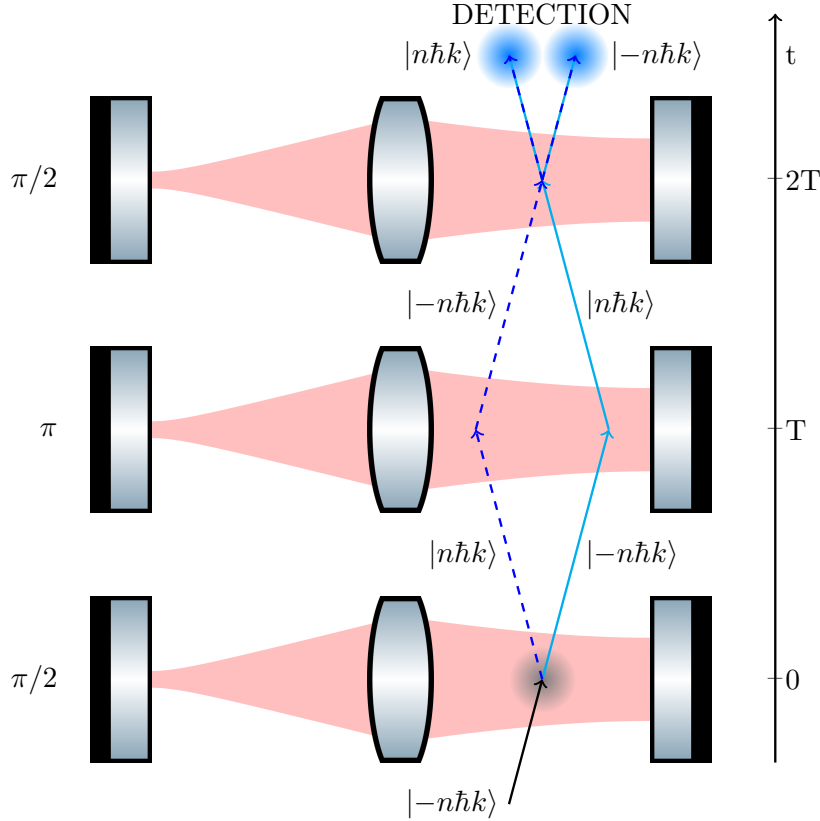


Figure 7. Cavity enhanced atomic accelerometer operated in microgravity. The atomic ensemble, initially at the mid point between the lens and the right mirror and with momentum $| -n\hbar k \rangle$, is split, deflected and recombined with cavity enhanced pulses in a Mach-Zehnder configuration.

For the sake of simplicity, we study an horizontal accelerometer configuration in microgravity [24] so that the same beam coherently manipulates the atoms with a three pulses sequence. The configuration is shown in Fig. 7. The atomic ensemble used in the interferometric sequence has a temperature of $1.0 \mu\text{K}$ in the two directions perpendicular to the cavity axis. The width of the velocity distribution along the interrogation direction is set to be much smaller than the recoil velocity so as to avoid the spatial overlap of the two interferometer output ports after the interferometer. This condition can be obtained with a long velocity selection pulse prior to the interferometric sequence. The same pulse can be used to set the initial velocity $v_0 = -n\hbar\mathbf{k}/M$ of the ensemble to fulfill the order n Bragg reflection condition with the standing wave created in the cavity injected with a single laser of wavevector \mathbf{k} . The position of the cloud at

the time of the first $\pi/2$ pulse is set to be at the center between the lens and the mirror M_2 .

3.2. Simulation

To numerically evaluate the effects of the fields inhomogeneities on the LMT interferometer in the configuration of Fig. 7, we consider an ensemble of atoms as two level systems with ground state $|g\rangle$ and excited state $|e\rangle$ (energy separation $\hbar\omega_{eg}$) interacting with two counter-propagating beams with frequency ω . We define $k = 2\pi/\lambda = \omega/c$ the optical wavevector of the laser, and $\Delta = \omega_{eg} - \omega$ the laser detuning with respect to the optical transition. The detuning Δ is assumed to be much larger than the linewidth of the excited state. In the Rotating Wave Approximation, and after adiabatic elimination of the excited state $|e\rangle$, the evolution of the state $|\Psi(t)\rangle = \sum_m a_m(t) |m\rangle$, where $|m\rangle \equiv |g, m\hbar\mathbf{k}\rangle$, in the laser field is given by a tri-diagonal Hamiltonian matrix H (see, e.g. Ref. [13]), with the diagonal terms given by the atom kinetic energy:

$$\langle m| H(t) |m\rangle = -m^2\hbar\omega_r \quad (15)$$

and the off-diagonal elements representing the coupling between the momentum states:

$$\langle m \pm 2| H(t) |m\rangle = \frac{\hbar\Omega(t)}{2} e^{\pm i\Delta\phi}. \quad (16)$$

Here $\omega_r = \hbar\mathbf{k}^2/2M$ is the single photon recoil frequency, and $\Omega = |E_c^+||E_c^-|/2\Delta$ the time-dependent two photon Rabi frequency. We evaluate numerically the evolution of the state $|\Psi(t)\rangle$ in the case of Gaussian pulses $\Omega(t) = \bar{\Omega}e^{-t^2/2\sigma^2}$, where $\bar{\Omega}$ is the peak Rabi frequency, since they have been shown to enhance the efficiency of LMT beam splitters [13, 25].

3.2.1. Zero temperature. We first consider the case of an atom at zero temperature interacting with a spatially homogeneous laser field, to recall that LMT Bragg diffraction requires large Rabi frequencies and enlighten the use of a cavity. In Fig. 8 we plot the transfer efficiency from the $|-5\rangle$ state to the $|+5\rangle$ state for different values of $\bar{\Omega}$, as a function of the pulse duration δt_{FWHM} . For low Rabi frequencies (< 50 kHz), no appreciable transfer is obtained to the target state (blue curve). Increasing the coupling (100 kHz - red curve) starts to couple the different momentum states. Further increasing the coupling (150 kHz - purple curve and 200 kHz - green curve) brings to the Bragg regime, where a Rabi oscillation between the two momentum states $|\pm 5\rangle$ is observed. High diffraction efficiencies in the Bragg regime are thus obtained when $\bar{\Omega} \times \delta t_{\text{FWHM}} \simeq 1$. These results are in agreement with previous studies (see, e.g. Fig. 7 of [13]).

To illustrate the advantage of the cavity build up, we calculate the required input laser power to achieve a Rabi frequency of 200 kHz. We consider atoms in the $|F = 1, m_F = 0\rangle$ state and σ^+ polarized light. The coupled states are therefore $F' = 1, 2$

and the effective Rabi frequency of the Bragg transition is

$$\bar{\Omega} = \frac{\Gamma^2}{2} \sqrt{\frac{I_c^+ I_c^-}{4I_{sat}^2}} \left(\frac{5}{24\Delta} + \frac{3}{24(\Delta + \Delta_2)} \right) \quad (17)$$

with $\Gamma \simeq 2\pi \times 6.06$ MHz the excited state linewidth, $I_{sat} = 1.67$ mW.cm⁻² the saturation intensity, I_c^\pm the intensity of the two counter propagating cavity fields, Δ the detuning from the first coupled state ($F' = 1$) and $\Delta_2 = 2\pi \times 157$ MHz the splitting between $F' = 1$ and $F' = 2$ [26]. Using the link between the intensity and the power for a gaussian beam of waist ω_0 , and introducing the cavity amplification factor G , this expression can be re-written as

$$\bar{\Omega} = \frac{\Gamma^2}{2I_{sat}} \frac{GP_{in}}{\pi\omega_0^2} \left(\frac{5}{24\Delta} + \frac{3}{24(\Delta + \Delta_2)} \right). \quad (18)$$

Considering a detuning $\Delta = 2\pi \times 5$ GHz and a cavity waist $\omega_0 = 5$ mm, a peak Rabi frequency of 200 kHz can then be achieved with an amplification factor $G = 100$ and an input power of $P_{in} = 2.2$ mW.

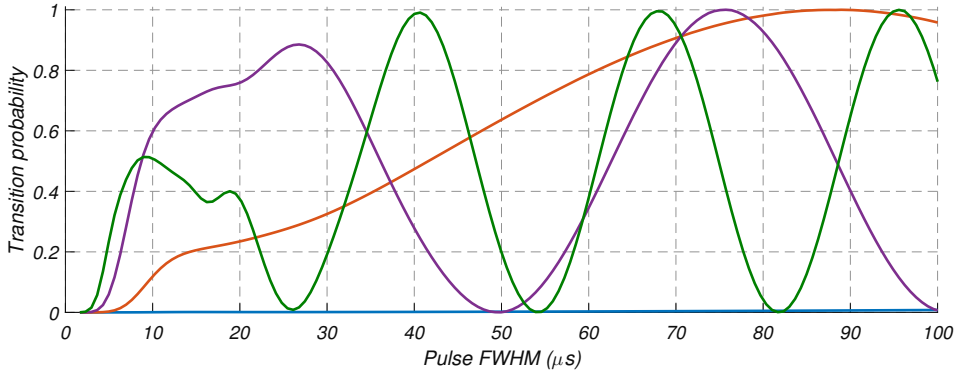


Figure 8. LMT Rabi oscillation for two different peak Rabi frequencies from state $|-5\rangle$ to $|+5\rangle$. We simulate gaussian pulses of varying duration, characterized by their Full Width Half Maximum (FWHM). The peak frequencies are 50 kHz (blue), 100 kHz (red), 150 kHz (purple) and 200 kHz (green).

3.2.2. Finite transverse temperature. We now study the LMT Bragg pulses in the cavity. We investigate the combined effect of the transverse velocity distribution of the atoms and the transverse profile of the interrogation laser beam on the Bragg diffraction efficiency. The expansion of the atomic cloud in the radial directions with respect to the interrogation beams is determined by the initial atomic temperature, set to 1 μ K. The velocity distribution along the interrogation direction is considered infinitely narrow so as to neglect Doppler effect; this condition is implemented experimentally by the use of a long velocity selection Bragg pulse before the interferometric sequence.

In Fig. 9 the coupling efficiency from the initial $|-5\rangle$ state to the $|+5\rangle$ state is studied for a pulse of variable duration and applied on the atomic ensemble after a free evolution of 100 ms, for different longitudinal misalignments δ_1 of mirror (M_1)

(Fig. 9(a)) and different peak Rabi frequencies (Fig. 9(b)). The results show that a transfer efficiency close to 100% is achievable in this resonator for $\delta_1 \leq 20\mu\text{m}$. The Rabi oscillations even improve when the cavity is slightly misaligned (orange and violet curves in Fig. 9(a)) because the intensity becomes more homogeneous than for a Gaussian beam (see Fig. 6). Then for larger misalignments, the important spatial inhomogeneity strongly degrades the Rabi oscillations. The simulations of Fig. 9(a) were performed by keeping a constant peak Rabi frequency equal to 200 kHz, although the optical gain decreases when the cavity is misaligned. The effect of reducing the Rabi frequency in a perfectly aligned cavity (Gaussian beam probed by the thermal atoms) is shown in Fig. 9(b) for comparison.

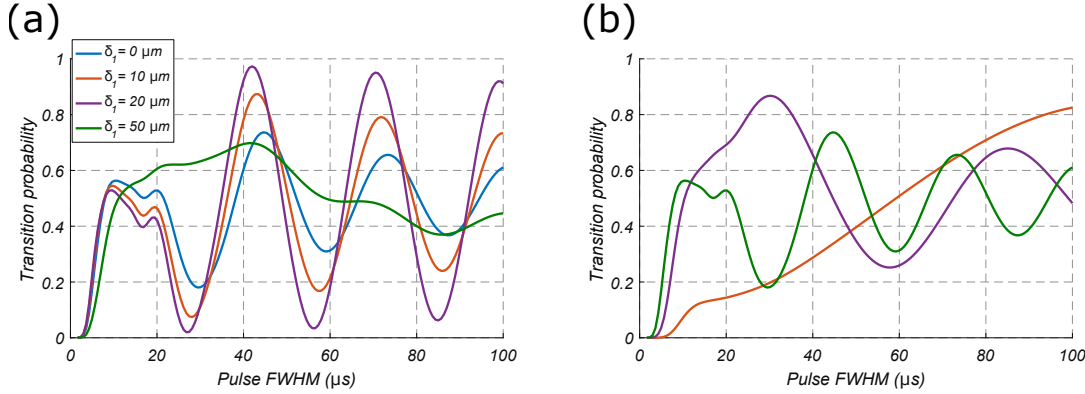


Figure 9. Rabi oscillation from the $|-5\rangle$ state to the $|+5\rangle$ state for an atom cloud with $1.0\ \mu\text{K}$ transverse temperature, after $100\ \text{ms}$ propagation time. (a) The different curves correspond to different longitudinal misalignments of the resonator with the peak Rabi frequency kept constant at 200 kHz. (b) The different curves correspond to different peak Rabi frequencies 100 kHz (red), 150 kHz (purple) and 200 kHz (green) in the case of a perfectly aligned cavity.

For the same atom-cavity assembly, we now consider a $\pi/2-\pi-\pi/2$ cavity-enhanced pulse sequence of total time $2T=100$ creating an atom Mach-Zehnder interferometer, as shown in Fig. 7. During each Bragg atom diffraction process of order n , the relative laser phase is imprinted n times on the matter-waves; the final phase shift for the whole interferometric sequence is thus

$$\Delta\Phi = n \times (\Delta\phi_1 - 2\Delta\phi_2 + \Delta\phi_3). \quad (19)$$

where $\Delta\phi_i$ is the relative phase of the lasers at the position of the atom during the i -th laser pulse [27]. The sensitivity to the inhomogeneities of the relative laser phase is thus n times higher. This could be a critical issue in relation to the longitudinal misalignment of the cavity elements, which modify the relative phase profile of the counter-propagating fields as presented in Fig. 6.

To evaluate the interferometric phase shift $\Delta\Phi$ in this configuration, we calculate the trajectory of each atom sampled out of a Gaussian thermal distribution of velocities corresponding to the temperature of $1\ \mu\text{K}$, and the imprinted position-dependent phase

shift. Fig. 10(a) shows the mean interferometer phase shift as a function of the input mirror misalignment. Fig. 10(b) shows the histograms of the phases imprinted on the atoms at the three Bragg pulses of the interferometer for the particular value $\delta_1 \sim 10 \mu\text{m}$, and (c) the histogram of the total phase shift $\Delta\Phi$ at the end of the interferometer calculated with Eq. (19). Fig. 10(a) shows that misalignments of the input mirror induce systematic phase shifts of few mrad only for δ_1 up to $20 \mu\text{m}$. Such systematic shifts can be characterized by changing the position of the input mirror or the temperature of the atoms. They are therefore not problematic for high precision interferometry.

The spread of the phase shifts (e.g. 21 mrad rms for $\delta_1 \sim 10 \mu\text{m}$) would lead to a systematic contrast reduction but this effect is negligible for misalignments δ_1 below $20 \mu\text{m}$. In our simulation, only the transverse variation of the relative laser phase is considered, and not the fact that atoms exploring the edge of the beam – where the Rabi frequency is lower – contribute less to the interferometer signal due to reduced transition probabilities. The calculated spread of the phase shift thus represents an upper bound and so the possible contrast reduction.

In conclusion, longitudinal misalignments do not significantly affect both the contrast and phase of the interferometer, making this resonator geometry compatible with precision interferometry based on LMT Bragg pulses.

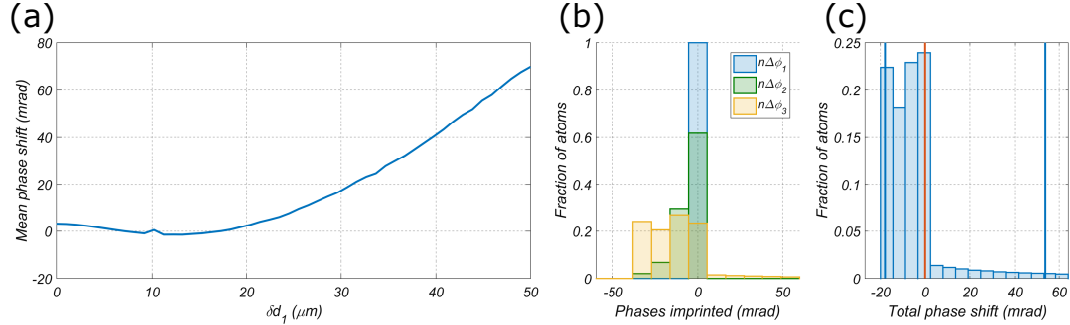


Figure 10. (a) Mean interferometer phase shift associated with the inhomogeneity of the relative phase of the counter propagating cavity fields caused by a misalignment of the cavity and the spread of the $1.0 \mu\text{K}$ atom cloud between the three interrogation pulses of a 200 ms long interferometer. (b) Histograms of the phases imprinted on the atoms at the three pulses for a $\delta_1 = 10 \mu\text{m}$ input mirror misalignment. (c) Histogram of the total interferometer phase shift for $\delta_1 = 10 \mu\text{m}$. The red line shows the mean phase shift and the blue lines show the 5% and 95% percentiles.

4. Conclusion

We proposed a marginally stable optical resonator suitable for atom interferometry applications. The resonator consists of two flat mirrors placed symmetrically at the focal planes of a lens and magnifies an input waist ω'_0 by a factor $\lambda f / (\pi \omega_0'^2)$. Waists of several millimeters in the second half of the resonator can be obtained with input

beams of $\omega'_0 \simeq 20 \mu\text{m}$ and focal length $f \simeq 40 \text{ cm}$. Optical gains of several hundreds can be obtained for a lens with losses of about 0.1% and standard high reflectivity mirrors. Such large beams are suitable for atom interferometry devices such as accelerometers, gradiometers or gyroscopes operating with thermal ($\sim \mu\text{K}$) atom sources. The power enhancement at resonance will enable to operate conventional or LMT atom interferometers with lower requirements on the input laser power. We investigated the robustness of the resonator to longitudinal misalignments in terms of phase and intensity profiles of the intra-cavity field, and illustrated its application to an atom interferometer based on $2 \times 5\hbar k$ LMT Bragg diffraction. High order LMT in the resonator could for example allow to operate cold atom inertial sensors at reduced interrogation times in order to increase their bandwidth [28] and reduce their volume.

Future works should focus on the effect of tilts of the optical elements, which can be simulated using generalized beam matrices [29], and on imperfections of the optical surfaces. Regarding LMT atom optics, the effect of diffraction phase shifts [30] and their control in this resonator geometry should be investigated.

Acknowledgments

This work was realized with the financial support of the French State through the “Agence Nationale de la Recherche” (ANR) in the frame of the “Investissement d’avenir” programs: Equipex MIGA (ANR-11-EQPX-0028), IdEx Bordeaux - LAPHIA (ANR-10-IDEX-03-02) and FIRST-TF (ANR-10-LABX-48-01). This work was also supported by the Région d’Aquitaine (project IASIG-3D) and by the city of Paris (Emergence project HSENS-MWGRAV). We also thank the “Pôle de compétitivité Route des lasers - Bordeaux” cluster for his support. G. L. thanks DGA for financial support. M. P. has been partly supported by LAPHIA–IdEx Bordeaux.

References

- [1] Herbert Walther, Benjamin T H Varcoe, Berthold-Georg Englert, and Thomas Becker. Cavity quantum electrodynamics. *Reports on Progress in Physics*, 69(5):1325–1382, apr 2006.
- [2] Serge Haroche. Nobel lecture: Controlling photons in a box and exploring the quantum to classical boundary. *Reviews of Modern Physics*, 85(3):1083–1102, jul 2013.
- [3] Helmut Ritsch, Peter Domokos, Ferdinand Brennecke, and Tilman Esslinger. Cold atoms in cavity-generated dynamical optical potentials. *Reviews of Modern Physics*, 85(2):553–601, apr 2013.
- [4] Kristian Baumann, Christine Guerlin, Ferdinand Brennecke, and Tilman Esslinger. Dicke quantum phase transition with a superfluid gas in an optical cavity. *Nature*, 464(7293):1301–1306, apr 2010.
- [5] Yves Colombe, Tilo Steinmetz, Guilhem Dubois, Felix Linke, David Hunger, and Jakob Reichel. Strong atom–field coupling for Bose–Einstein condensates in an optical cavity on a chip. *Nature*, 450(7167):272–276, nov 2007.
- [6] Kevin C. Cox, Graham P. Greve, Joshua M. Weiner, and James K. Thompson. Deterministic squeezed states with collective measurements and feedback. *Phys. Rev. Lett.*, 116(9), mar 2016.

- [7] Onur Hosten, Nils J. Engelsen, Rajiv Krishnakumar, and Mark A. Kasevich. Measurement noise 100 times lower than the quantum-projection limit using entangled atoms. *Nature*, 529(7587):505–508, jan 2016.
- [8] Paul Hamilton, Matt Jaffe, Justin M. Brown, Lothar Maisenbacher, Brian Estey, and Holger Müller. Atom interferometry in an optical cavity. *Phys. Rev. Lett.*, 114(10), mar 2015.
- [9] Holger Müller, Sheng wey Chiow, Quan Long, Sven Herrmann, and Steven Chu. Atom interferometry with up to 24-photon-momentum-transfer beam splitters. *Physical Review Letters*, 100(18), may 2008.
- [10] T. Lévêque, A. Gauguier, F. Michaud, F. Pereira Dos Santos, and A. Landragin. Enhancing the area of a Raman atom interferometer using a versatile double-diffraction technique. *Phys. Rev. Lett.*, 103(8), aug 2009.
- [11] Sheng wey Chiow, Tim Kovachy, Hui-Chun Chien, and Mark A. Kasevich. $102\hbar k$ large area atom interferometers. *Phys. Rev. Lett.*, 107(13), sep 2011.
- [12] G. D. McDonald, C. C. N. Kuhn, S. Bennetts, J. E. Debs, K. S. Hardman, M. Johnsson, J. D. Close, and N. P. Robins. $80\hbar k$ momentum separation with bloch oscillations in an optically guided atom interferometer. *Physical Review A*, 88(5), nov 2013.
- [13] Holger Müller, Sheng wey Chiow, and Steven Chu. Atom-wave diffraction between the Raman-Nath and the Bragg regime: Effective Rabi frequency, losses, and phase shifts. *Phys. Rev. A*, 77(2), feb 2008.
- [14] Anne Louchet-Chauvet, Tristan Farah, Quentin Bodart, André Clairon, Arnaud Landragin, Sébastien Merlet, and Franck Pereira Dos Santos. The influence of transverse motion within an atomic gravimeter. *New Journal of Physics*, 13(6):065025, 2011.
- [15] I. Dutta, D. Savoie, B. Fang, B. Venon, C.L. Garrido Alzar, R. Geiger, and A. Landragin. Continuous cold-atom inertial sensor with 1 nrad/sec rotation stability. *Phys. Rev. Lett.*, 116(18), may 2016.
- [16] B Fang, I Dutta, P Gillot, D Savoie, J Lautier, B Cheng, C L Garrido Alzar, R Geiger, S Merlet, F Pereira Dos Santos, and A Landragin. Metrology with atom interferometry: inertial sensors from laboratory to field applications. *ArXiv:1601.06082*, January 2016.
- [17] C Freier, M Hauth, V Schkolnik, B Leykauf, M Schilling, H Wziontek, H-G Scherneck, J Müller, and A Peters. Mobile quantum gravity sensor with unprecedented stability. *J. Phys.: Conf. Ser.*, 723:012050, jun 2016.
- [18] H. Kogelnik and T. Li. Laser beams and resonators. *Appl. Opt.*, 5(10):1550, oct 1966.
- [19] A E Siegman. *Lasers*. University Science Books, 1986.
- [20] J. L. Hall, C. J. Bordé, and K. Uehara. Direct optical resolution of the recoil effect using saturated absorption spectroscopy. *Physical Review Letters*, 37(20):1339–1342, nov 1976.
- [21] A E Siegman. Unstable optical resonators. *Appl. Opt.*, 13(2):353–367, 1974.
- [22] M. Fatih Erden and Haldun M. Ozaktas. Accumulated Gouy phase shift in Gaussian beam propagation through first-order optical systems. *Journal of the Optical Society of America A*, 14(9):2190, sep 1997.
- [23] B. Canuel, S. Pelisson, L. Amand, A. Bertoldi, E. Cormier, B. Fang, S. Gaffet, R. Geiger, J. Harms, D. Holleville, A. Landragin, G. Lefèvre, J. Lhermite, N. Mielec, M. Prevedelli, I. Riou, and P. Bouyer. Miga: combining laser and matter wave interferometry for mass distribution monitoring and advanced geodesy, 2016.
- [24] R. Geiger, V. Menoret, G. Stern, N. Zahzam, P. Cheinet, B. Battelier, A. Villing, F. Moron, M. Lours, Y. Bidel, A. Bresson, A. Landragin, and P. Bouyer. Detecting inertial effects with airborne matter-wave interferometry. *Nat Commun*, 2:474–, sep 2011.
- [25] E. Giese, A. Roura, G. Tackmann, E. M. Rasel, and W. P. Schleich. Double Bragg diffraction: A tool for atom optics. *Physical Review A*, 88(5), nov 2013.
- [26] Daniel A Steck. Rubidium 87 d line data, 2001.
- [27] Mark Kasevich and Steven Chu. Atomic interferometry using stimulated raman transitions. *Physical Review Letters*, 67(2):181–184, jul 1991.

- [28] Akash V. Rakholia, Hayden J. McGuinness, and Grant W. Biedermann. Dual-axis high-data-rate atom interferometer via cold ensemble exchange. *Phys. Rev. Applied*, 2(5), nov 2014.
- [29] Anthony A. Tovar and Lee W. Casperson. Generalized beam matrices: Gaussian beam propagation in misaligned complex optical systems. *Journal of the Optical Society of America A*, 12(7):1522, jul 1995.
- [30] M. Büchner, R. Delhuille, A. Miffre, C. Robilliard, J. Vigué, and C. Champenois. Diffraction phases in atom interferometers. *Physical Review A*, 68(1), jul 2003.

Appendix A. Calculation of the cavity amplification factor G .

We note in the following E_{in} the incident field on the cavity, E_{cM_1} the stationary intra cavity field of power P_{cM_1} propagating in the forward direction on mirror (M_1) and ϕ the optical phase acquired after one round trip in the resonator. We also note r_1, r_2, r_L and t_1, t_2, t_L the amplitude reflection and transmission coefficients of respectively (M_1), (M_2) and (l) that we consider without losses. The interference between the cavity waves on (M_1) reads (see Fig. A1):

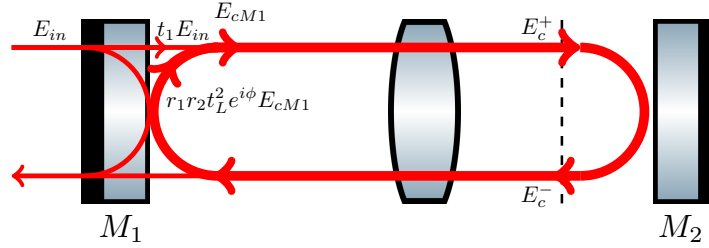


Figure A1. E_{cM_1} is the stationary intra-cavity field propagating in the forward direction on mirror (M_1). The field $r_1r_2t_L^2e^{i\phi}E_{cM_1}$ is the same field after one round trip inside the cavity. The field t_1E_{in} is the incident field leaking inside the resonator.

$$E_{cM_1} = t_1E_{\text{in}} + r_1r_2t_L^2e^{i\phi}E_{cM_1}. \quad (\text{A.1})$$

At resonance, $e^{i\phi}=1$, we have therefore:

$$E_{cM_1} = \frac{t_1}{(1 - r_1r_2t_L^2)}E_{\text{in}} \quad (\text{A.2})$$

which means

$$P_{cM_1} = \frac{1 - r_1^2}{(1 - r_1r_2(1 - r_L^2))^2}P_{\text{in}} \quad (\text{A.3})$$

Considering that $P_c^- = r_2^2P_c^+$, the amplification factor of the cavity can be written:

$$G = r_2 \frac{P_c^+}{P_{\text{in}}} = r_2 \frac{P_c^+}{P_{cM_1}} \frac{P_{cM_1}}{P_{\text{in}}} = (1 - r_L^2) \frac{P_{cM_1}}{P_{\text{in}}} \quad (\text{A.4})$$

We therefore obtain:

$$G = \frac{r_2(1 - r_1^2)(1 - r_L^2)}{(1 - r_1r_2(1 - r_L^2))^2}. \quad (\text{A.5})$$

This expression stands for a perfectly aligned resonator. The optical gain will decrease from this maximum value when the cavity is misaligned. We obtain $G=100$ for the cavity parameters set in Sec. 2.2.

The Finesse of the resonator can be calculated considering small variations of the frequency around resonance and developing Eq. A.1 at first order:

$$\mathcal{F} = \frac{\pi \sqrt{r_1 r_2 (1 - r_L^2)}}{1 - r_1 r_2 (1 - r_L^2)}. \quad (\text{A.6})$$

Appendix B. Details of the numerical calculation of the fields $E_c^\pm(r, z)$

We give here details on the convergence of the calculation of the field (Eq. (14)). We iterate the round trips to a number that equals four times the finesse \mathcal{F} , which allows for a convergence of the field amplitude and phase for all r to less than 10^{-6} . More precisely, writing $E_{[k]}(r, z) = \sum_{n=1}^k E_n(r, z)$ and

$$\rho_{||}(r, z) = \frac{||E_{[k+1]}(r, z)| - |E_{[k]}(r, z)||}{|E_{[k]}(r, z)|} \quad (\text{B.1})$$

$$\rho_\varphi(r, z) = ||\arg(E_{[k+1]}(r, z)) - \arg(E_{[k]}(r, z))||, \quad (\text{B.2})$$

we observe at the end of the calculation that $\max_r(\rho_{||}(r, z)) < 10^{-6}$ and $\max_r(\rho_\varphi(r, z)) < 10^{-6}$.

In order to lock the cavity we run the circulating field calculation for a set of different input wavelength and record the gain. We chose 50 wavelengths regularly spaced in one free spectral range. This number allows us to find at least one wavelength on the resonance for finesse up to 1000. We find the wavelength with maximal gain and run the calculation again with a new set of wavelength around this maximum. We repeat this process a few times until the wavelength step $\Delta\lambda$ is below 10^{-9} nm. This number, accounting for the 80 cm long cavity and 780 nm wavelength gives us a precision on the pointing of the resonance down to 10^{-5} of the free spectral range of the cavity. This is sufficient for finesse of a few hundreds ($\mathcal{F} = 355$ for the cavity parameters set in Sec. 2.2).

Appendix C. Misalignment of the output mirror

Fig. C1 shows the effect of the misalignment of the output mirror (M_2) on the interrogation field. When the input mirror (M_1) is perfectly aligned, the displacement of (M_2) has nearly no effect on the circulating field (see Fig. C1(a)). When (M_1) is misaligned for a value of $20 \mu\text{m}$, (M_2) has to be misaligned by at least a few millimetres to get a significant modification of the circulating field in the cavity.

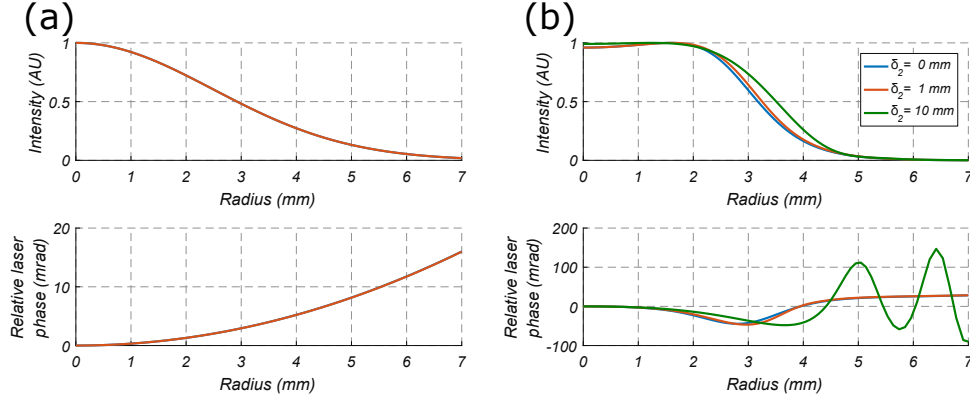


Figure C1. Circulating field in the cavity when misaligning the output mirror (M_2). The upper plots show the radial intensity profile of the cavity field $E_c^+(r, z)$ at the middle point z between the lens and the mirror (M_2). The lower plots show the radial profile of the relative phase $\Delta\phi(r, z)$ between the two counter-propagating cavity fields $E_c^+(r, z)$ and $E_c^-(r, z)$. (a) The input mirror (M_1) is perfectly aligned, the output mirror (M_2) is misaligned by 0 mm (blue) and 1 mm (red), the lines are superimposed. (b) (M_1) is misaligned by 20 μm and (M_2) by 0 mm (blue), 1 mm (red) and 10 mm (green).